http://pubs.acs.org/journal/aelccp

Fluorinated Cyclic Ether Diluent for High-Voltage Lithium Metal Batteries

Kyunam Lee,[†] Sun-Hyun Kwon,[†] Jisub Kim, Eunseok Park, Inwoo Kim, Hyo Chul Ahn, Ali Coskun,* and Jang Wook Choi*

ABSTRACT: Although localized high-concentration electrolytes (LHCEs) show promising performance with lithium metal anodes, LHCEs do not necessarily stabilize the interface with state-of-the-art high-voltage cathodes. Here, we report a functional diluent, 2,2-bis(trifluoromethyl)-1,3-dioxolane (BTFMD), to demonstrate LHCEs for high-voltage lithium metal batteries (LMBs), which stabilizes the cathode and anode interfaces simultaneously through distinct mechanisms. The fluorinated cyclic ketal moiety of BTFMD, along with diminished free solvent formation, enables oxidative stability as high as 6.0 V vs Li/Li$^+$. Additionally, BTFMD undergoes self-decomposition to produce lithium fluoride and induces an anion-dominant solvation structure to establish an inorganic-rich solid electrolyte interphase. Incorporation of BTFMD diluent realized a Coulombic efficiency of 99.54% in a Li|Cu cell and 80% capacity retention for Li|LiNi$_{0.8}$Co$_{0.1}$Mn$_{0.1}$O$_2$ full-cells after 570 and 250 cycles, with cutoff voltage levels of 4.3 and 4.4 V, respectively. This study highlights the usefulness of fluorinated diluents and their controlled solvation structures for high-voltage LMBs.

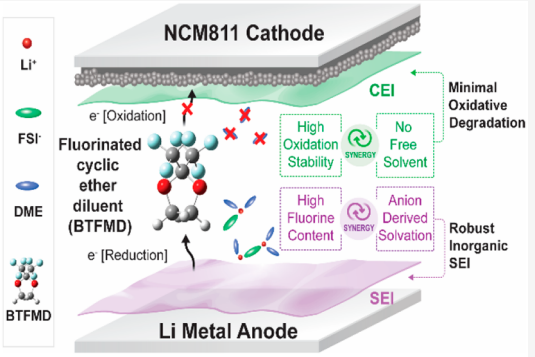

Attempts to keep pace with the ever-evolving specifications of portable electronics and electric vehicles have encouraged the battery community to explore advanced battery systems beyond lithium-ion batteries (LIBs), particularly in terms of the energy density.[1,2] Lithium metal batteries (LMBs) are well aligned with this objective owing to the high specific capacity (3860 mAh g^{-1}) and the lowest redox potential (−3.04 V vs the standard hydrogen electrode) of the lithium metal anode (LMA).[3,4] However, the application of LMBs is generally hindered by their short cycle life and unwarranted safety, which originate from indiscriminate dendritic growth and consequent electrolyte decomposition.[5−7] These failure modes are directly related to the characteristics of the solid electrolyte interphase (SEI) on the LMA; for example, an SEI layer rich in organic components is usually less protective against the aforementioned failure behaviors compared with its inorganic-rich counterparts. Even worse is that the SEI formed by conventional carbonate electrolytes is not sufficiently stable to realize LMBs with a fairly long cycle life.[8,9] In this regard, researchers in the community have developed a variety of strategies such as employing solid-state electrolytes,[10,11] artificial SEI layers,[12,13] three-dimensional host designs,[14,15] and electrolyte additives.[16,17] Among these available options, liquid electrolyte engineering is preferred over the other approaches because it can be integrated into current cell manufacturing processes with minimal adjustments.[18,19]

Ether-based electrolytes offer relatively higher compatibility with the LMA as a result of their enhanced reductive stability, as is typically reflected in the lesser extent of solvent degradation and lower organic content of the SEI.[20] However, further stabilization of the SEI is desirable because ethers alone do not guarantee long-term cyclability. Ethers also have the disadvantage of insufficient oxidative stability and are thus difficult to pair with state-of-the-art high-voltage Li$Ni_xCo_yMn_zO_2$ (NCM) cathodes.[21] In an effort to proceed beyond ethers, researchers have focused on the solvation structure around the Li ion because an anion-involved solvation structure can induce a more sustainable, inorganic-rich SEI layer on the LMA. Recently reported high-concentration electrolytes,[22,23] localized high-concentration electrolytes (LHCEs),[24−26] and weakly solvating electrolytes[27,28] are representative strategies to realize these anion-

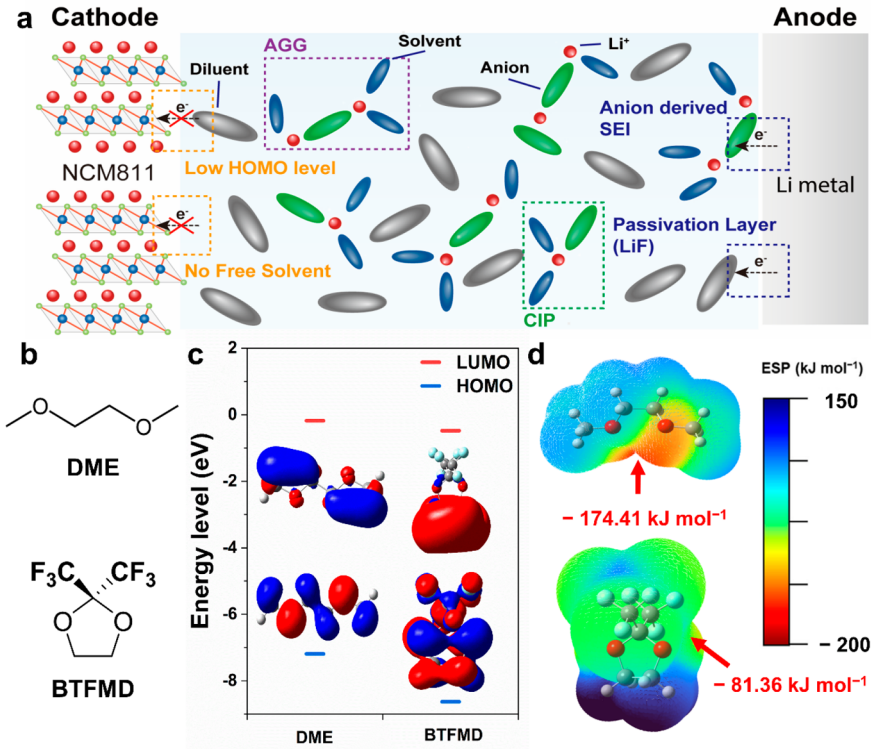

Figure 1. (a) Schematic illustration of the LHCE design with different stabilizing mechanisms for the cathode and anode. (b) Chemical structures of DME (solvent) and BTFMD (diluent). (c) Calculated energy levels of HOMO−LUMO and molecular orbital diagrams. (d) Calculated minimum electrostatic potential (ESP) maps for DME and BTFMD. Color scheme: sky blue, F; red, O; gray, C; white, H. Regions of negative and positive charge are indicated in red and blue, respectively.

involved solvation structures. In the same context, in terms of their ion configuration, anion-containing solvation structures predominantly constitute contact ion pairs (CIP) and aggregated ions (AGG) rather than solvent-separated ion pairs (SSIP). LHCEs have been highlighted with discernible attention because they predominantly form the CIP and AGG configurations, all while maintaining moderate salt concentrations and viscosity, which sets them apart from HCEs.[29,30] The diluents in LHCEs are typically miscible with the main solvents without solvating the Li ions. This explains the extensive utilization of highly fluorinated ethers.[28,31,32] However, recent studies have revealed that these diluents may not be as inert as was previously assumed. Instead, they have been discovered to undergo decomposition at the interfaces on both sides of the electrodes, thereby contributing to the formation of the SEI and the cathode electrolyte interphase (CEI).[33] This observation implies that it is essential to consider the (electro)chemical reactions of diluents at the electrode surfaces, despite the fact that this perspective has not been extensively reflected in the design of LHCEs.

In this study, we introduce commercially available 2,2-bis(trifluoromethyl)-1,3-dioxolane (BTFMD) as a functional diluent for LHCE-based LMBs. The cyclic ketal structure, typically used as a protective group in organic synthesis, contained two electron-withdrawing trifluoromethyl groups to endow the diluent with high oxidative stability.[34] From the viewpoint of the solvation structure, the presence of this diluent induces a structure predominantly composed of AGG, which contributes to a lithium fluoride (LiF)-rich, stable SEI on the LMA. Taking advantage of these beneficial properties, 2 M bis(fluorosulfonyl)imide (LiFSI) in 1,2-dimethoxyethane (DME)/BTFMD (v/v = 1:3) gave an average Coulombic efficiency (CE) of 99.54% for Li plating/stripping in a Li|Cu cell. Furthermore, the extraordinary oxidative stability indicated by the near absence of an anodic current up to 6.0 V vs Li/Li^+ allows BTFMD-based LHCEs to deliver highly stable cycling performance in a full-cell with Li-$Ni_{0.8}Co_{0.1}Mn_{0.1}O_2$ (NCM811): 82.2% capacity retention for 570 cycles when cycled at 1C with a cutoff voltage of 4.3 V.

Electrolyte Design and Characterization. Owing to the chemical inertness derived from their strong carbon−fluorine bonds, fluorinated ethers have found a wide range of applications such as heat transfer media, cleaning solvents for electronic devices, and anesthetics for medical use.[35] The electron-withdrawing nature of fluorine also confers low solvation power and high oxidative stability. Furthermore, fluorinated ethers are generally miscible with DME, a common ether-based solvent for LMBs, thereby making them suitable for use as diluents for LHCEs. Although considered to be "inert", these diluents have been discovered to decompose under electrochemical bias. Particularly, because an excess of diluent is present within the electrolyte without participating in solvation, further enhancement of the stability of fluorinated ethers is desired. The oxidative stability could generally be improved by substituting electron-withdrawing groups (EWGs) to lower the highest occupied molecular orbital (HOMO) level, although minimization of the molecular size would be a more effective approach to preserving the viscosity and wettability in the desirable ranges. Moreover, as the HOMO level is lowered with the addition of EWGs, the lowest unoccupied molecular orbital (LUMO) level is also depressed, consequently weakening the reductive stability. Thus, a new diluent design capable of overcoming these trade-offs is highly desired.

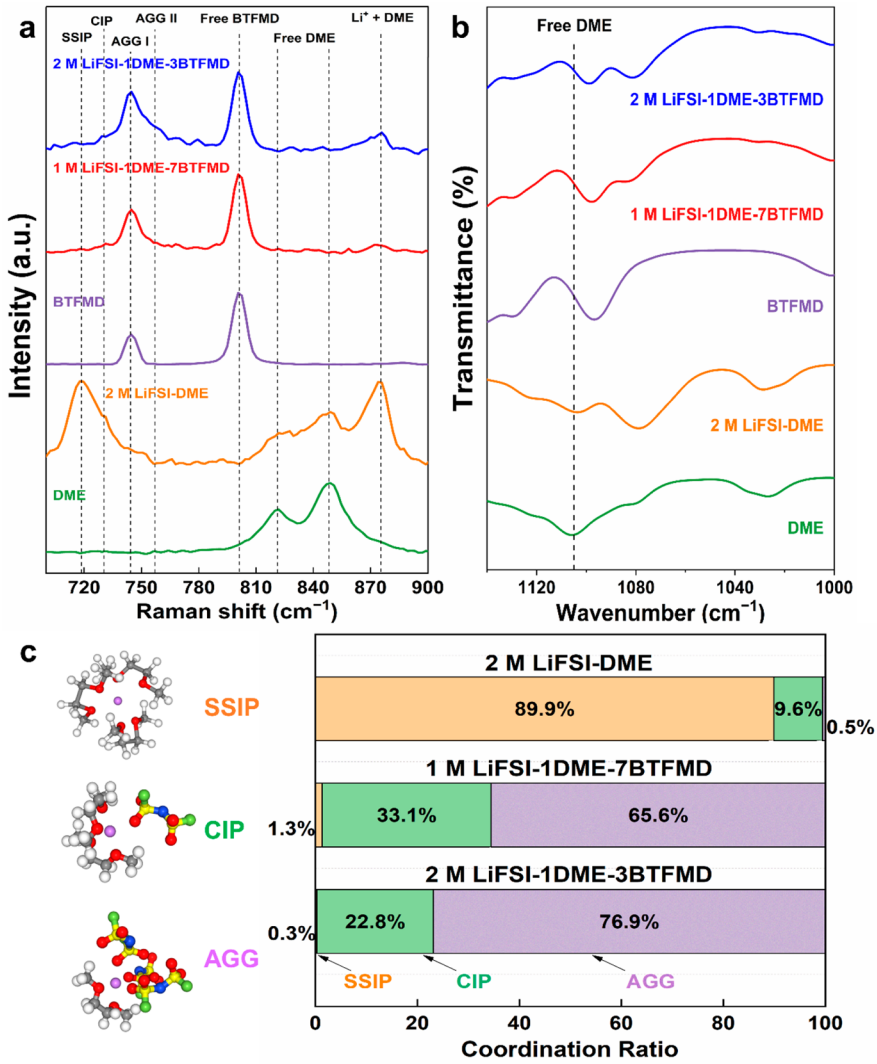

Figure 2. (a) Raman and (b) FT-IR results for solvation structure analysis of solvents and electrolytes. (c) Images of probable solvation structures and their contents in different electrolytes from molecular dynamics (MD) simulations.

We hypothesized that these trade-offs could be resolved through diluent design by utilizing reductive decomposition to create a passivation layer on the LMA (Figure 1a). Previously, a range of fluorinated molecules was demonstrated to be suitable as diluents because fluorination weakens the energy of the neighboring oxygen and nitrogen atoms for coordination with Li ions, whereas the decomposed molecules can induce the desired LiF-containing components in the SEI layer. In this direction, fluorinated aromatic[36] and ether[37−41] compounds proved to be the most remarkable. Additionally, a majority of these compounds also have the benefit of reinforcing the oxidative stability. In the present investigation, we introduce commercially available BTFMD (Figure 1b) as a functional diluent with high oxidative stability. The oxidative stability of this molecule is attributed to the presence of the two electron-withdrawing trifluoromethyl groups combined with its inherently stable cyclic ketal structure (Figure S1). The significantly lower HOMO level (−8.63 eV) of BTFMD, suggested by density functional theory (DFT) calculations, compared to that of DME (−7.19 eV) supports the enhanced oxidative stability of BTFMD (Figure 1c). The incorporation of EWGs ensures a low LUMO level of −0.48 eV; additionally, the high fluorine content of BTFMD, which exceeds 50% of its molecular weight, beneficially acts as a source for the formation of a LiF-rich inorganic SEI during its reductive decomposition. In addition, we calculated the minimum electrostatic potential (ESP) values of DME and BTFMD to estimate their solvation ability (Figure 1d).[39] Because the trifluoromethyl groups withdraw the electron cloud from the oxygen atoms, BTFMD is expected to have bare solvation ability (the minimum ESP of −81.36 kJ mol^{-1}) compared to DME (the minimum ESP of −174.41 kJ mol^{-1}), thereby supporting the role of BTFMD as a diluent.

We investigated the chemical reactivity of BTFMD with LMA by immersing Li metal foil in the diluent for 24 h. The black appearance of the surface of the immersed Li metal (Figure S2a) is consistent with previous studies involving fluorinated aromatic diluents.[36] The surface components of the blackened Li metal were characterized by carrying out X-ray photoelectron spectroscopy (XPS) analysis. Except for the organic C−F at 688.5 eV during the initial period of sputtering, F 1s profiles were depth-independent and displayed a LiF peak at 684.8 eV (Figure S2b). This result confirms the ability of BTFMD to form an inorganic SEI during its reductive

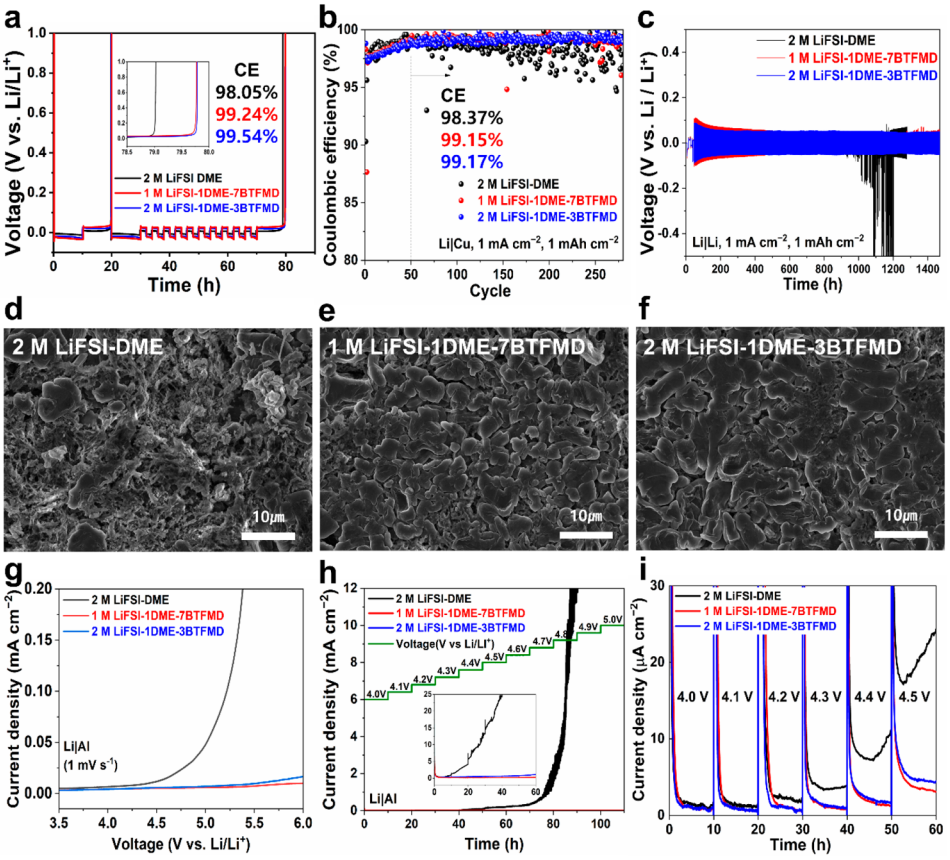

Figure 3. (a) Aurbach measurements in Li|Cu cells. (b) CE tests of asymmetric Li|Cu cells with different electrolytes cycled at 1.0 mA cm^{-2}. The average CE was calculated with the CE values after 50 cycles. (c) Voltage−time profiles of Li|Li symmetric cells with different electrolytes cycled at 1.0 mA cm^{-2} and 1.0 mAh cm^{-2}. Scanning electron microscopy (SEM) images of Li surfaces plated on the Cu current collectors after cycling in (d) 2 M LiFSI-DME, (e) 1 M LiFSI-1DME-7BTFMD, and (f) 2 M LiFSI-1DME-3BTFMD during the 5th cycle. Oxidative stability tests in Li|Al asymmetric cells examined by (g) linear sweep voltammetry (LSV) with a scan rate of 1.0 mV s^{-1} and (h) potentiostatic polarization tests in the range of 4.0−5.0 V with a voltage increment of 0.1 V at time intervals of 10 h. (i) Potentiostatic profiles of Li|NCM811 cells with a voltage increment of 0.1 V at time intervals of 10 h.

decomposition. Moreover, the immersion of Li metal foil in the LHCE containing BTFMD for 1 day barely changed the color (Figure S2c), suggesting that, after the passivation of the Li metal foil with the preferential decomposition of the anion in the LHCE, the Li foil is protected from further reaction with BTFMD. Nonetheless, should the electrolyte encounter a more reductive environment during cell operation, the diluent would decompose to uncover its role as an additive of sorts; the decomposition of BTFMD itself would additionally contribute to the formation of an inorganic-rich SEI, which would significantly enhance the stability of the LMA.

Solvation Structure Analysis. BTFMD was combined with DME and LiFSI for utilization as an LHCE. To investigate the effect of the salt concentration and diluent volume ratio on the LMB performance, we dissolved 1 and 2 M LiFSI in DME and BTFMD at volume ratios of 1:7 and 1:3, respectively (referred to as 1 M LiFSI-1DME-7BTFMD and 2 M LiFSI-1DME-3BTFMD, respectively). Notably, both electrolytes shared the same molar ratio of Li salt to DME (1:1) so that the effect of the relative portions of DME and BTFMD could be explicitly determined. The fixed Li salt-to-DME ratio induces consistent local environments in the inner solvation shell. As a control electrolyte, a 2 M LiFSI salt dissolved in DME (referred to as 2 M LiFSI-DME) was prepared.

We employed Raman spectroscopy to elucidate the solvation structures in the different electrolytes (Figure 2a). The Raman spectrum of 2 M LiFSI-DME is characterized by a high-intensity peak at 719.0 cm^{-1}, which corresponds to the S−N−S bending of the solvent-separated FSI anion, indicating a solvation structure mainly composed of SSIP.[42,43] In contrast, the peak corresponding to SSIP was hardly observed in LHCEs with BTFMD, whereas the new peak detected at 747 cm^{-1}, corresponded to AGG-I (FSI$^-$ coordinating to two Li$^+$ ions) solvation structure.[44] Moreover, the shoulder peak at 760 cm^{-1}, which is more prominent in 2 M LiFSI-1DME-3BTFMD, indicated the presence of AGG-II (FSI$^-$ coordinating to more than two Li$^+$ ions) solvation structures.[45] The intensity of both peaks of 2 M LiFSI-1DME-3BTFMD was higher than that of 1 M LiFSI-1DME-7BTFMD, indicating a more pronounced presence of the anion-rich solvation structures in 2 M LiFSI-1DME-3BTFMD despite the consistent local environments of the inner solvation shell.

Free DME, which does not participate in Li$^+$ solvation, is susceptible to oxidative degradation and should thus be minimized in the electrolyte for high-voltage NCM cathodes for operation in a cell. The presence of a significant amount of free DME in 2 M LiFSI-DME was evident from the characteristic peaks at 820 and 850 cm^{-1}.[46,47] In contrast, the absence of these peaks for the 1 M LiFSI-1DME-7BTFMD

and 2 M LiFSI-1DME-3BTFMD electrolytes suggests a near-complete coordination of DME molecules with Li^+ ions. In addition, Fourier-transform infrared (FT-IR) spectroscopy revealed a distinct peak corresponding to free DME (around 1100 cm^{-1}) in the 2 M LiFSI-DME solution, whereas it was absent from the two BTFMD-based LHCEs (Figure 2b).[48]

Molecular dynamics (MD) simulations were performed to investigate the solvation structure and validate the results obtained from Raman and FT-IR spectroscopy. In the case of 2 M LiFSI-DME, the average coordination number of DME for the Li^+ ion was significantly higher at 2.87, compared to the average coordination of FSI^- of 0.11, indicating the prevalence of the SSIP structure (Figures 2c and S3). Conversely, for 1 M LiFSI-1DME-7BTFMD and 2 M LiFSI-1DME-3BTFMD, the average coordination numbers of DME for the Li^+ ion were both 1.00 (Figures S4 and S5), which implies that nearly all of the DME molecules are coordinating with Li^+ ions. The average coordination values of FSI^- were 2.51 and 2.56 for 1 M LiFSI-1DME-7BTFMD and 2 M LiFSI-1DME-3BTFMD, respectively, indicating that the majority of FSI^- anions form AGG structures with Li^+ ions (Figure 2c). The negligible coordination values of 0.05 and 0.03 for BTFMD confirmed that it acts as a diluent in the LHCEs. In addition, MD simulations revealed that 2 M LiFSI-1DME-3BTMD has a higher percentage of AGG solvation structures compared to 1 M LiFSI-1DME-7BTMD (Figure 2c), which is consistent with the Raman spectroscopy results (see Figure 2a).

Despite both 1 M LiFSI-1DME-7BTFMD and 2 M LiFSI-1DME-3BTFMD being primarily composed of the AGG solvation structure with almost no SSIP, they had decent ionic conductivities (2.36 and 3.57 mS cm^{-1}, respectively), similar to those of reported LHCEs (Tables S1 and S2). This might be related to the small molecular size and moderate density of BTFMD (d_{BTFMD} = 1.53 g cm^{-3}) originating from its cyclic structure, despite its high fluorine content. Notably, contact angle measurements indicated improved wettability between the separator and the BTFMD-based electrolytes compared to that of 2 M LiFSI-DME (Figure S6). This property of the BTFMD-based electrolytes is likely to be beneficial for reducing dendrite formation by ensuring uniform electrolyte distribution and thus Li-ion flux.[49]

Performance and Morphology Analyses in Various Cell Configurations. To investigate the effects of the AGG-enriched solvation structures of the BTFMD-based electrolytes and the functionality of BTFMD itself, we conducted comprehensive electrochemical tests in various cell configurations such as Li|Cu and Li|Al half-cells, Li|Li symmetric cells, and full-cells paired with NCM811 cathodes.

The compatibility of the electrolyte with LMA is largely influenced by the formation of the SEI layer in relation to electrolyte decomposition. We performed cyclic voltammetry (CV) measurements with the Li|Cu half-cell in the range of 1.5−0.0 V vs Li/Li^+ and compared the cathodic current to examine the decomposition behavior of the different electrolytes (Figure S7). During the initial voltage scan from open-circuit voltage (OCV) to 1.0 V, all three electrolytes had two similar cathodic peaks, mainly from anion decomposition. However, in the voltage range below 1.0 V, where solvent decomposition predominates, the current response of the BTFMD-based LHCEs was smaller compared to that of 2 M LiFSI-DME.[50] This can be interpreted as indicating that the BTFMD-based LHCEs formed a robust SEI layer in the early stage of electrolyte decomposition, thereby minimizing solvent decomposition. The low and minimal variation in the cathodic current over subsequent cycles of the LHCEs also verifies the formation of a robust SEI. In addition, Aurbach's method was used in a Li|Cu half-cell configuration to probe the average CE associated with Li plating and stripping.[51] 1 M LiFSI-1DME-7BTFMD and 2 M LiFSI-1DME-3BTFMD exhibited higher average CEs of 99.24% and 99.54% compared to 98.05% of 2 M LiFSI-DME (Figure 3a). The compatibility of both LHCEs with Li metal improved significantly compared to that of 2 M LiFSI-DME, although a notable difference existed between them, even though both possess similar AGG-enriched solvation structures. This could be attributed not only to the higher AGG content of 2 M LiFSI-1DME-3BTFMD, but also to the promoted decomposition of anions as a result of its greater portion of the AGG-II structure compared to that in 1 M LiFSI-1DME-7BTFMD (see Figure 2a).[45] Furthermore, the higher ionic conductivity of 2 M LiFSI-1DME-3BTFMD and the resulting lower plating/stripping overpotentials may have contributed to this difference.[39]

The enhanced cathodic reversibility of the BTFMD-based electrolytes also contributed to the cycling performance of the Li|Cu half-cells, leading to higher average CEs for 250 cycles of Li plating/stripping at a current density of 1.0 mA cm^{-2} and the areal capacity of 1 mAh cm^{-2} in comparison with the DME-based electrolyte (99.17% and 99.15%, respectively, compared to 98.37%) (Figure 3b). The improved stability of Li|Li symmetric cells with the BTFMD-based electrolytes compared with 2 M LiFSI-DME can be understood similarly. Whereas stable cycling for over 1400 h was observed with 2 M LiFSI-1DME-3BTFMD at 1.0 mA cm^{-2} and 1.0 mAh cm^{-2}, the cell containing 2 M LiFSI-DME experienced a severe increase in overpotential and ceased to operate at approximately 900 h under the same cell conditions (Figure 3c).

Scanning electron microscopy (SEM) analysis was additionally employed to explore the influence of electrolytes on the morphology of the plated Li. Li was plated on Cu foil at the capacity of 1 mAh cm^{-2} and current density of 1 mA cm^{-2} with three different electrolytes. The Li plating on the Cu substrate with 2 M LiFSI-DME exhibited various detrimental features such as cracks, Li filaments, and exposed Cu substrate, all of which represent nonuniform coverage of Li plating and undesirable side reactions with the electrolyte (Figure 3d). In contrast, Li plating in 1 M LiFSI-1DME-7BTFMD was characterized by a uniform distribution of chunky Li grains with minimal gaps (Figure 3e). Moreover, in the case of 2 M LiFSI-1DME-3BTFMD, the morphology of the plated Li was further improved with enhanced flatness and larger Li grains, along with reduced crack formation (Figure 3f). Cross-sectional SEM analysis also revealed a stark contrast in the plated Li morphologies among the different electrolytes (Figure S8). 2 M LiFSI-DME displayed uncontrolled Li filament growth, whereas the BTFMD-based electrolytes exhibited large Li grains with small surface areas. Once again, the synergistic effect of the primary decomposition of the anion and the subsequent decomposition of BTFMD were found to play a crucial role in achieving the observed uniform Li metal plating through the formation of a LiF-rich SEI layer.

The effect of the oxidative stability of BTFMD based on its low HOMO level (−8.63 eV) was investigated by conducting linear sweep voltammetry (LSV) measurements using Li|Al asymmetric cells from the OCV to 6.0 V vs Li/Li^+ at a scan rate of 1.0 mV s^{-1}. The 2 M LiFSI-DME started decomposing at approximately 4.2 V, whereas the BTFMD-based electro-

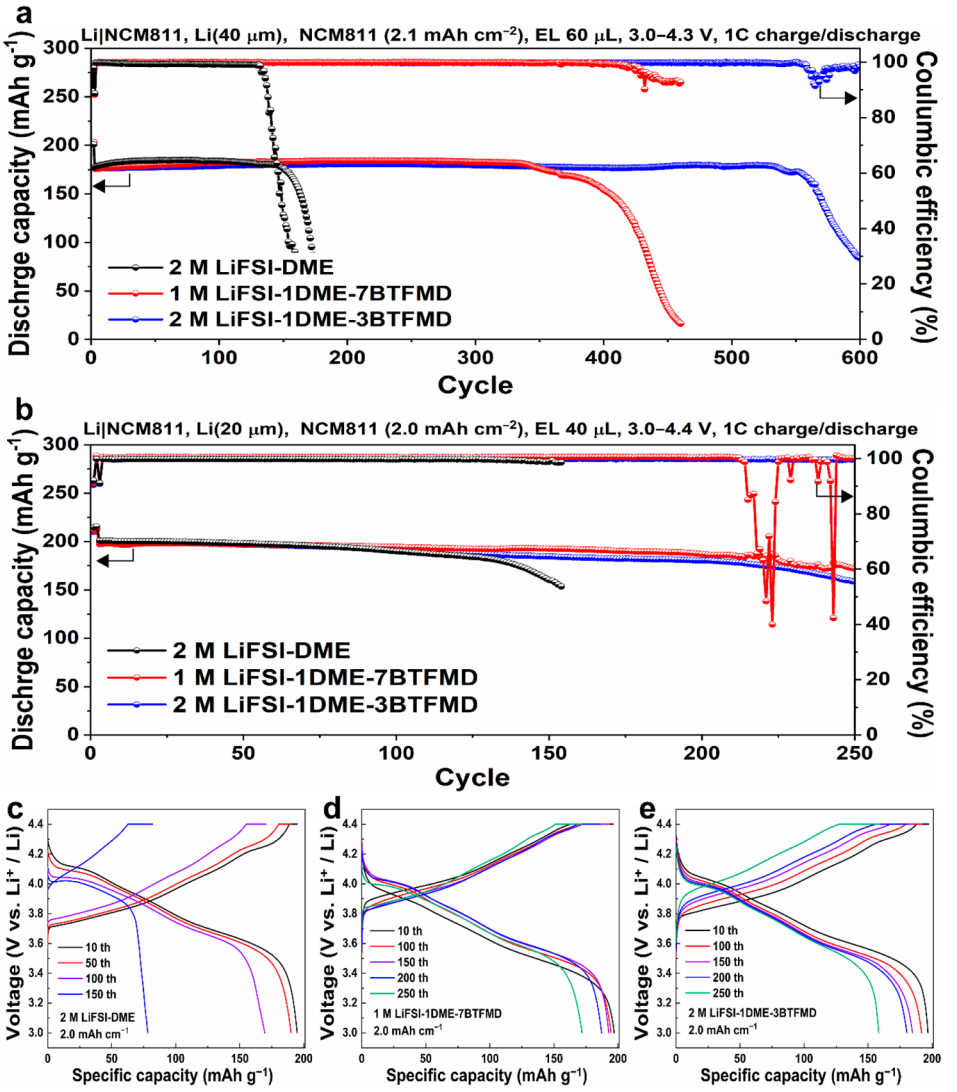

Figure 4. Cycling performance of Li|NCM811 full-cells at 1C (0.2 A g^{-1}) across different voltage ranges: (a) 3.0−4.3 V and (b) 3.0−4.4 V, after two formation cycles at 0.1C. Charge−discharge profiles of Li|NCM811 full-cells at different cycles with (c) 2 M LiFSI-DME, (d) 1 M LiFSI-1DME-7BTFMD, and (e) 2 M LiFSI-1DME-3BTFMD in the voltage range 3.0−4.4 V.

lytes did not undergo significant decomposition up to nearly 5.5 V (Figure 3g). On the other hand, LiFSI-based electrolytes are reportedly responsible for severely corroding the Al current collector.[52,53] To examine this corrosion issue, potentiostatic polarization tests were performed on Li|Al cells ranging from 4.0 to 5.0 V at a 0.1 V interval, with each voltage level maintained for 10 h (Figure 3h). In the case of 2 M LiFSI-DME, the exponential increase in the anodic current around 4.2 V reflects its low oxidative stability in relation to its weak tolerance for corrosion. In contrast, the anodic current of the BTFMD-based electrolytes was hardly significant at all until 4.5 V. Exposure of the Al current collector of the 2 M LiFSI-DME cell to 4.4 V for 40 h led to the formation of severe cracks due to corrosion on the Al surface (Figure S9a). In stark contrast, the Al current collectors in cells with the BTFMD-based electrolytes exhibited a flat and smooth surface with only a few pits (Figure S9b,c). The continuous exposure of the native aluminum surface to the electrolyte has been reported as the origin for aluminum corrosion in LiFSI-based electrolytes owing to the dissolution of $Al(FSI)_3$ that forms at a high voltage. However, in the BTFMD-based electrolytes, free solvent molecules are scarcely available for dissolving $Al(FSI)_3$, which once again highlights the importance of controlling the solvation structure of the Li^+ ion.

The oxidative stability of the electrolytes was also examined in the Li|NCM811 full-cell setting (Figure 3i). Starting from 4.0 V, the voltage applied to the full-cell was increased by 0.1 V with each voltage step being held for 10 h while monitoring the current flow. Consistent with the Li|Al asymmetric cell tests, the 2 M LiFSI-DME cell exhibited significantly higher leakage current at 4.2 V compared to the cells with BTFMD. Even though the leakage current in the BTFMD-based electrolytes increased with increasing voltage, the current levels were far lower than that of 2 M LiFSI-DME. This low leakage current is ascribed to their high oxidative stability, enhanced compatibility with the Al current collector, and minimal structural degradation of NCM811 during deep charging (*vide infra*). The series of experiments coherently demonstrated the superior oxidative stability of the BTFMD-based electrolytes and their usefulness in pairing with high-voltage cathodes.

As a consequence of the enhanced Li metal compatibility and oxidative stability of the BTFMD-based electrolytes, stable

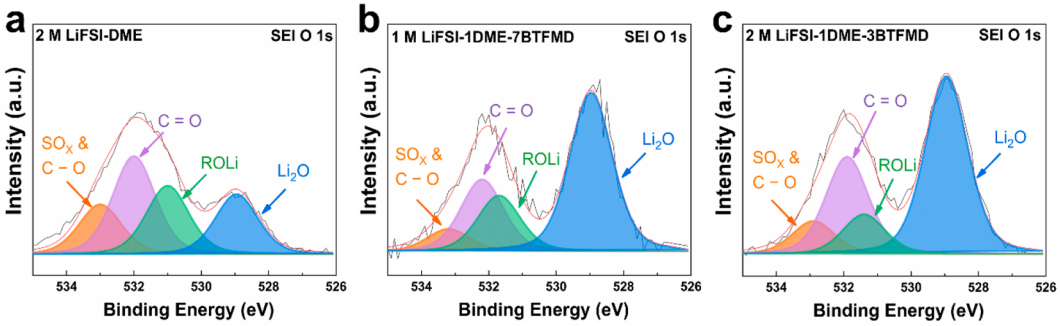

Figure 5. Ex situ interfacial analysis of the anode from Li|NCM811 cells after 3 cycles (2 formation cycles at 4.3 V followed by 1 cycle at 4.4 V). O 1s spectra of the SEI layers on the Li anodes after 1 min sputtering: (a) 2 M LiFSI-DME, (b) 1 M LiFSI-1DME-7BTFMD, and (c) 2 M LiFSI-1DME-3BTFMD.

cycling of the Li|NCM811 full-cells could also be demonstrated, in line with the aforementioned measurements. Figure 4a shows the full-cell performance of the BTFMD-based electrolytes with 40 μm-thick Li foil over the operating voltage range from 3.0 to 4.3 V. Both electrolytes containing BTFMD displayed stable cycling over 300 cycles at 1C, whereas the cell with 2 M LiFSI-DME stopped cycling after 130 cycles. Notably, even the two BTFMD-containing electrolytes differed significantly in terms of their cycling stability; the cell with 2 M LiFSI-1DME-3BTFMD sustained over 570 cycles with 82.2% capacity retention (141.1 mAh g^{-1}), whereas the cell with 1 M LiFSI-1DME-7BTFMD retained only 80% of its initial capacity after 413 cycles. Considering that both BTMFD-based electrolytes are stable with the NCM811 cathode at 4.3 V (Figure 3i), the distinct cyclability is likely to result from the superior reversibility of 2 M LiFSI-1DME-3BTFMD during repeated Li plating/stripping cycles (Figure 3a).

The performance of the BTFMD-based electrolytes was assessed under conditions that more closely resemble those used in practical cells by evaluating the Li|NCM811 full-cells with 20 μm-thick Li foil with an elevated cutoff voltage of 4.4 V (Figure 4b). Even at this high voltage level, the cells with 1 M LiFSI-1DME-7BTFMD and 2 M LiFSI-1DME-3BTFMD preserved excellent cycling stability with 87.0% and 80.3% capacity retention after 250 cycles, respectively. In contrast, the cell with 2 M LiFSI-DME ceased to operate after 150 cycles. Interestingly, the 1 M LiFSI-1DME-7BTFMD cell outperformed the 2 M LiFSI-1DME-3BTFMD cell with respect to the cycling stability when the upper cutoff voltage was increased from 4.3 to 4.4 V (Figure 4b). This phenomenon resulted from the higher oxidative stability of 1 M LiFSI-1DME-7BTFMD compared to 2 M LiFSI-1DME-3BTFMD although the Li plating/stripping reversibility in 1 M LiFSI-1DME-7BTFMD is inferior. These findings revealed the importance of balancing the interfacial stability on both sides of the electrodes. We expanded cell tests to anode-less Cu|NCM811 full-cells to see the versatility of the BTFMD-based electrolyte designs. Consistent with the results of the full-cells that implemented Li foil, the 2 M LiFSI-1DME-7BTFMD-based anode-less cell exhibited the best performance (Figures S10 and S11). In addition, the rate capability of the BTFMD-based electrolytes was evaluated over the voltage range from 3.0 to 4.4 V by varying the C-rate from 0.5 to 2.0C (Figure S12). Although the capacity difference between the two BTFMD-based electrolytes was insignificant up to 1C, the noticeable difference at 2C is ascribed to the higher ionic conductivity and enhanced interfacial stability of 2 M LiFSI-1DME-3BTFMD.

Interface Characterization. To identify the origin of the enhanced performance of the BTFMD-containing electrolytes, the SEI and CEI layers in the Li|NCM811 full-cells were subjected to X-ray photoelectron spectroscopy (XPS) analysis after operating for three cycles. XPS depth profiles were obtained through Ar^+ ion sputtering to explore the variation in the vertical composition of the SEI layers (Figure S13a–c). The BTFMD-based electrolytes were found to have a lower carbon concentration and a higher oxygen and fluorine concentration compared to those of 2 M LiFSI-DME, thereby reflecting the formation of anion-derived and LiF-rich SEI layers by the BTFMD-based electrolytes. In particular, the lowest carbon concentration (~5 atom %) in the SEI layer formed by 2 M LiFSI-1DME-3BTFMD, which demonstrated the highest average CE of 99.54% in the Li|Cu half-cell (see Figure 3a), can be correlated with its robust inorganic-rich composition. Additionally, the depth profile in Figure S13c indicates the depth-independent uniformity of the SEI layer on Li metal with 2 M LiFSI-1DME-3BTFMD.

Previous LHCE studies showed that the formation of Li_2O by the decomposition of the FSI^- anion is of crucial importance for Li plating/stripping efficiency.[39,54] The organic oxygen species that were predominantly found in the SEI layer formed by 2 M LiFSI-DME (Figure 5a) pointed to the prevalent formation of organic species. The XPS depth profiles of 2 M LiFSI-DME (Figure S14a) suggest nonuniformity along the depth, particularly in the outer layer. Contrary to this, the SEI layers formed by the BTFMD-based electrolytes gave rise to prominent Li_2O peaks at 529 eV (Figure 5b and c), and they had uniform distributions in the depth direction (Figure S14b,c). Furthermore, the Li 1s depth profiles supported the high Li_2O content and the homogeneous distribution thereof in the SEI layers driven by the BTFMD based electrolytes (Figure S15a–c). Another important inorganic SEI component, LiF, also differed distinctly in terms of its content. Whereas the LiF content was only about ~4 atom % in the SEI formed by 2 M LiFSI-DME, it reached ~6 atom % in 1 M LiFSI-1DME-7BTFMD and ~7 atom % in 2 M LiFSI-1DME-3BTFMD (Figures S13a–c and S14d–f). This almost 2-fold increase in the LiF content highlights the effectiveness of our electrolyte design, specifically the AGG-dominant ion configuration, as well as the involvement of diluent degradation. The S 2p spectra are also in line with the aforementioned results in terms of anion-driven decomposition and homogeneity along the depth (Figure S16a–c).

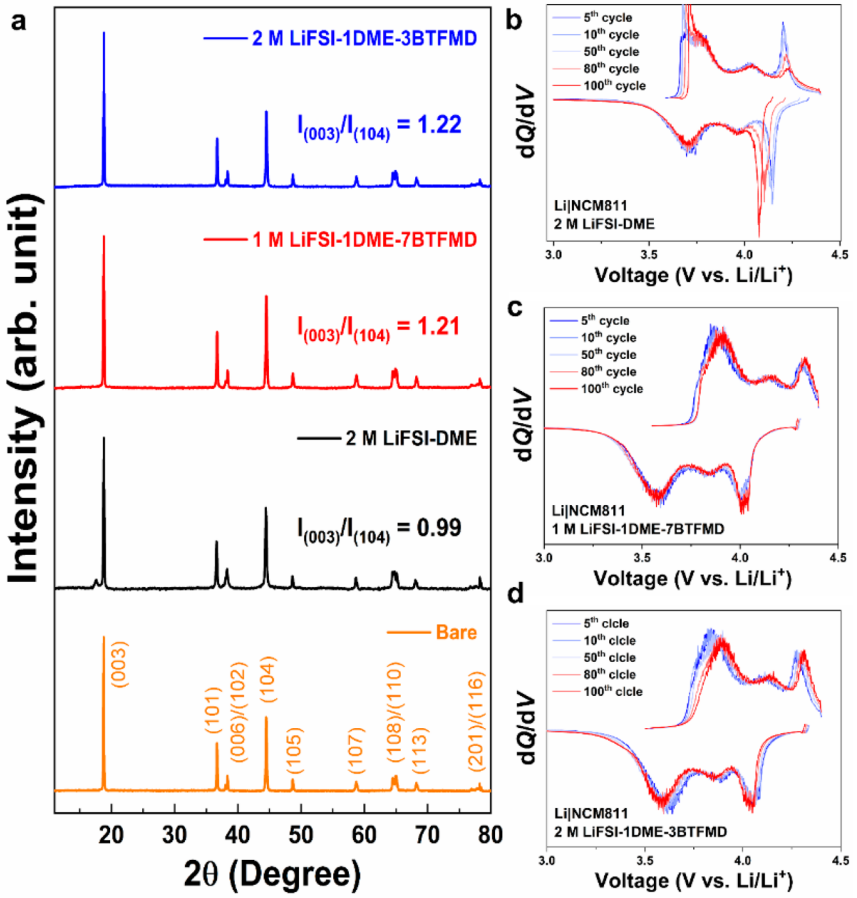

Figure 6. (a) X-ray diffraction (XRD) patterns of NCM811 cathodes from Li|NCM811 full-cells after 100 cycles in different electrolytes. d*Q*/d*V* profiles of Li|NCM811 full-cells at different cycles with (b) 2 M LiFSI-DME, (c) 1 M LiFSI-1DME-7BTFMD and (d) 2 M LiFSI-1DME-3BTFMD.

XPS analysis was also employed to assess the oxidative stability of BTFMD-based electrolytes on the NCM811 surface. The F 1s spectra revealed that the peak intensities of LiF at 684.8 eV in the CEI layers of NCM811 cycled in the BTFMD-based electrolytes were higher than those in the CEI formed by 2 M LiFSI-DME (Figure S17a–c). Moreover, the ratio of PVDF to LiF changed significantly along the depth in the case of 2 M LiFSI-DME, whereas that of the BTFMD-based electrolytes did not change notably, indicating the formation of a rather homogeneous CEI layer. Additionally, the depth profiles of the O 1s species revealed that the metal oxide peaks at 529.6 eV evolved more rapidly with Ar^+ ion sputtering for the CEI formed by the BTFMD-based electrolytes compared to 2 M LiFSI-DME (Figure S17d–f). The results indicate that a thinner CEI layer was formed on NCM811 in the presence of the BTFMD-based electrolytes. The superior oxidative stability of the BTFMD-based electrolytes and the formation of the robust LiF-rich CEI layers could therefore be concluded to have effectively suppressed additional electrolyte decomposition.

Cathode Stability and Degradation Analysis. Using X-ray diffraction (XRD) analysis, we further verified the effect of stabilization of the cathode interface by the BTFMD-based electrolytes on suppressing the degradation of the NCM811 cathode. To assess the structural integrity, the crystallinity of the cathode was evaluated after 100 cycles with different electrolytes (Figure 6a). Interfacial destabilization induced by the dissolution of transition metal ions, is one of the major degradation pathways of the NCM811 cathodes and leads to cation substitution by the migration of Ni^{2+} ions into the layered Li^+ sites.[55,56] Because the intensity ratio of the (003) and (104) peaks, denoted as $I(003)/I(104)$, decreases with an increasing cation substitution, we used this ratio as an indicator of the degree of cathode degradation. The much higher $I(003)/I(104)$ of the cathode with the BTFMD-based electrolytes (1.21 for 1 M LiFSI-1DME-7BTFMD and 1.22 for 2 M LiFSI-1DME-3BTFMD) compared to 0.99 for 2 M LiFSI-in-DME clearly verified that the BTFMD-based electrolytes successfully suppressed the degradation of NCM811 during cycling.

In addition to XRD analysis, the dQ/dV profiles of the Li|NCM811 full-cell were recorded for 100 cycles to assess the state of health (SoH) of the cathodes. Typically, Ni-rich cathodes such as NCM811 undergo a series of phase transitions (H1 → M → H2 → H3) during charging, which can be observed as distinct peaks on the d*Q*/d*V* profiles.[57,58] The NCM811 cathode becomes vulnerable to degradation through the H2 → H3 transition during deep charging, which results in a sudden lattice contraction in the *c*-direction and significant volume changes.[59] The cathode cycled in 2 M LiFSI-DME displayed severe peak broadening and an intensity decrease at ~4.2 V with repeated charge–discharge due to the irreversibility of the H2 → H3 transition (Figure 6b). Remarkably, the reversible phase transition, which includes

the H2 → H3 transition, in the cathodes cycled in the LHCEs based on BTFMD was retained over 100 cycles (Figure 6c,d). Accordingly, it can be inferred that the BTFMD-based LHCEs preserved the crystalline structure of the high voltage cathodes by virtue of their notable oxidative stability and the ability to form a robust CEI layer.

In summary, we introduced a novel fluorinated diluent, 2,2-bis(trifluoromethyl)-1,3-dioxolane (BTFMD), to enable LHCEs to operate reliably in high-voltage LMBs. The ability of this diluent to form LiF through decomposition to subsequently passivate the Li metal surface successfully overcame the trade-off between oxidative and reductive stability during fluorine substitution. In addition, its use in the LHCE realized AGG-rich solvation structures with no free DME and thus compatibility with both high-voltage NCM811 and LMA. Interestingly, 2 M LiFSI-1DME-3BTFMD offered significantly high oxidation resistance against NCM811 at 4.4 V vs Li/Li^+ and simultaneously supported high lithium plating/stripping reversibility with 99.54% CE in a Li|Cu cell. This work clearly underlines the importance of considering the functions of diluents when designing LHCEs to ensure stability at the interfaces on both sides of the electrodes with their significantly different electrochemical environments. We anticipate these findings on the functional fluorinated diluent to shorten the way to the practical implementation of LMBs.

■ ASSOCIATED CONTENT

Supporting Information

The Supporting Information is available free of charge at https://pubs.acs.org/doi/10.1021/acsenergylett.4c00481.

Experimental details, MD calculation results, SEM images, XPS results, material characterization results, and additional electrochemical results (PDF)

■ AUTHOR INFORMATION

Corresponding Authors

Ali Coskun − *Department of Chemistry, University of Fribourg, Fribourg 1700, Switzerland;* orcid.org/0000-0002-4760-1546; Email: ali.coskun@unifr.ch

Jang Wook Choi − *School of Chemical and Biological Engineering and Institute of Chemical Processes, Seoul National University, Seoul 08826, Republic of Korea;* orcid.org/0000-0001-8783-0901; Email: jangwookchoi@snu.ac.kr

Authors

Kyunam Lee − *School of Chemical and Biological Engineering and Institute of Chemical Processes, Seoul National University, Seoul 08826, Republic of Korea*

Sun-Hyun Kwon − *School of Chemical and Biological Engineering and Institute of Chemical Processes, Seoul National University, Seoul 08826, Republic of Korea*

Jisub Kim − *School of Chemical and Biological Engineering and Institute of Chemical Processes, Seoul National University, Seoul 08826, Republic of Korea*

Eunseok Park − *School of Chemical and Biological Engineering and Institute of Chemical Processes, Seoul National University, Seoul 08826, Republic of Korea;* orcid.org/0000-0001-9756-9532

Inwoo Kim − *School of Chemical and Biological Engineering and Institute of Chemical Processes, Seoul National University, Seoul 08826, Republic of Korea;* orcid.org/0000-0003-1442-0236

Hyo Chul Ahn − *School of Chemical and Biological Engineering and Institute of Chemical Processes, Seoul National University, Seoul 08826, Republic of Korea*

Complete contact information is available at: https://pubs.acs.org/10.1021/acsenergylett.4c00481

Author Contributions

†K.L. and S.-H.K. contributed equally to this work.

Notes

The authors declare no competing financial interest.

■ ACKNOWLEDGMENTS

J.W.C. acknowledges financial support from the National Research Foundation of Korea (Grant NRF-2021R1A2B5B03001956), the Technology Innovation Program (20012341) funded by the Ministry of Trade, Industry & Energy (MOTIE) of Korea, and generous support from the Institute of Engineering Research (IOER) and the Research Institute of Advanced Materials (RIAM) at Seoul National University.

■ REFERENCES

(1) Liu, J.; Bao, Z. N.; Cui, Y.; Dufek, E. J.; Goodenough, J. B.; Khalifah, P.; Li, Q. Y.; Liaw, B. Y.; Liu, P.; Manthiram, A.; et al. Pathways for practical high-energy long-cycling lithium metal batteries. *Nat. Energy* **2019**, *4* (3), 180−186.

(2) Choi, J. W.; Aurbach, D. Promise and reality of post-lithium-ion batteries with high energy densities. *Nat. Rev. Mater.* **2016**, *1* (4), 16013.

(3) Kwon, T. W.; Choi, J. W.; Coskun, A. Prospect for Supramolecular Chemistry in High-Energy-Density Rechargeable Batteries. *Joule* **2019**, *3* (3), 662−682.

(4) Xu, W.; Wang, J.; Ding, F.; Chen, X.; Nasybulin, E.; Zhang, Y.; Zhang, J.-G. Lithium metal anodes for rechargeable batteries. *Energy Environ. Sci.* **2014**, *7* (2), 513−537.

(5) Zhang, X.; Yang, Y.; Zhou, Z. Towards practical lithium-metal anodes. *Chem. Soc. Rev.* **2020**, *49* (10), 3040−3071.

(6) Sun, X.; Zhang, X.; Ma, Q.; Guan, X.; Wang, W.; Luo, J. Revisiting the Electroplating Process for Lithium-Metal Anodes for Lithium-Metal Batteries. *Angew. Chem., Int. Ed.* **2020**, *59* (17), 6665−6674.

(7) Lin, D.; Liu, Y.; Cui, Y. Reviving the lithium metal anode for high-energy batteries. *Nat. Nanotechnol.* **2017**, *12* (3), 194−206.

(8) Park, J. B.; Choi, C.; Yu, S.; Chung, K. Y.; Kim, D. W. Porous Lithiophilic Li-Si Alloy-Type Interfacial Framework via Self-Discharge Mechanism for Stable Lithium Metal Anode with Superior Rate. *Adv. Energy Mater.* **2021**, *11* (37), No. 2101544.

(9) Wang, H. S.; Liu, Y. Y.; Li, Y. Z.; Cui, Y. Lithium Metal Anode Materials Design: Interphase and Host. *Electrochem. Energy Rev.* **2019**, *2* (4), 509−517.

(10) Wang, C.; Adair, K.; Sun, X. All-Solid-State Lithium Metal Batteries with Sulfide Electrolytes: Understanding Interfacial Ion and Electron Transport. *Acc. Mater. Res.* **2022**, *3* (1), 21−32.

(11) Wang, C.; Gong, Y.; Liu, B.; Fu, K.; Yao, Y.; Hitz, E.; Li, Y.; Dai, J.; Xu, S.; Luo, W.; et al. Conformal, Nanoscale ZnO Surface Modification of Garnet-Based Solid-State Electrolyte for Lithium Metal Anodes. *Nano Lett.* **2017**, *17* (1), 565−571.

(12) Chen, C.; Liang, Q. W.; Wang, G.; Liu, D. D.; Xiong, X. H. Grain-Boundary-Rich Artificial SEI Layer for High-Rate Lithium Metal Anodes. *Adv. Funct. Mater.* **2022**, *32* (4), No. 2107249.

(13) Li, X. R.; Lv, M. M.; Tian, Y.; Gao, L.; Liu, T. F.; Zhou, Q. H.; Xu, Y. F.; Shen, L.; Shi, W. Y.; Li, X. Y.; et al. Negatively charged polymeric interphase for regulated uniform lithium-ion transport in stable lithium metal batteries. *Nano Energy* **2021**, *87*, No. 106214.

(14) Eom, K.; Jung, J.; Lee, J. T.; Lair, V.; Joshi, T.; Lee, S. W.; Lin, Z. Q.; Fuller, T. F. Improved stability of nano-Sn electrode with high-quality nano-SEI formation for lithium ion battery. *Nano Energy* **2015**, *12*, 314−321.
(15) Chen, H.; Yang, Y. F.; Boyle, D. T.; Jeong, Y. K.; Xu, R.; de Vasconcelos, L. S.; Huang, Z. J.; Wang, H. S.; Wang, H. X.; Huang, W. X.; et al. Free-standing ultrathin lithium metal-graphene oxide host foils with controllable thickness for lithium batteries. *Nat. Energy* **2021**, *6* (8), 790−798.
(16) Zheng, J. M.; Engelhard, M. H.; Mei, D. H.; Jiao, S. H.; Polzin, B. J.; Zhang, J. G.; Xu, W. Electrolyte additive enabled fast charging and stable cycling lithium metal batteries. *Nat. Energy* **2017**, *2* (3), 17012.
(17) Peng, Z.; Cao, X.; Gao, P. Y.; Jia, H. P.; Ren, X. D.; Roy, S.; Li, Z. D.; Zhu, Y.; Xie, W. P.; Liu, D. Y.; et al. High-Power Lithium Metal Batteries Enabled by High-Concentration Acetonitrile-Based Electrolytes with Vinylene Carbonate Additive. *Adv. Funct. Mater.* **2020**, *30* (24), No. 2001285.
(18) Liu, S.; Ji, X.; Yue, J.; Hou, S.; Wang, P.; Cui, C.; Chen, J.; Shao, B.; Li, J.; Han, F.; et al. High Interfacial-Energy Interphase Promoting Safe Lithium Metal Batteries. *J. Am. Chem. Soc.* **2020**, *142* (5), 2438−2447.
(19) Zhou, T. H.; Zhao, Y.; El Kazzi, M.; Choi, J. W.; Coskun, A. Stable Solid Electrolyte Interphase Formation Induced by Monoquat-Based Anchoring in Lithium Metal Batteries. *ACS Energy Lett.* **2021**, *6* (5), 1711−1718.
(20) Fang, C.; Li, J.; Zhang, M.; Zhang, Y.; Yang, F.; Lee, J. Z.; Lee, M. H.; Alvarado, J.; Schroeder, M. A.; Yang, Y.; et al. Quantifying inactive lithium in lithium metal batteries. *Nature* **2019**, *572* (7770), 511−515.
(21) Zhang, W.; Lu, Y.; Wan, L.; Zhou, P.; Xia, Y.; Yan, S.; Chen, X.; Zhou, H.; Dong, H.; Liu, K. Engineering a passivating electric double layer for high performance lithium metal batteries. *Nat. Commun.* **2022**, *13* (1), 2029.
(22) Qian, J.; Henderson, W. A.; Xu, W.; Bhattacharya, P.; Engelhard, M.; Borodin, O.; Zhang, J. G. High rate and stable cycling of lithium metal anode. *Nat. Commun.* **2015**, *6*, 6362.
(23) Yamada, Y.; Wang, J.; Ko, S.; Watanabe, E.; Yamada, A. Advances and issues in developing salt-concentrated battery electrolytes. *Nat. Energy* **2019**, *4* (4), 269−280.
(24) Chen, S.; Zheng, J.; Mei, D.; Han, K. S.; Engelhard, M. H.; Zhao, W.; Xu, W.; Liu, J.; Zhang, J. G. High-Voltage Lithium-Metal Batteries Enabled by Localized High-Concentration Electrolytes. *Adv. Mater.* **2018**, *30* (21), No. e1706102.
(25) Li, T.; Li, Y.; Sun, Y. L.; Qian, Z. F.; Wang, R. H. New Insights on the Good Compatibility of Ether-Based Localized High-Concentration Electrolyte with Lithium Metal. *ACS Energy Lett.* **2021**, *3* (6), 838−844.
(26) Lin, S.; Hua, H.; Li, Z.; Zhao, J. Functional Localized High-Concentration Ether-Based Electrolyte for Stabilizing High-Voltage Lithium-Metal Battery. *ACS Appl. Mater. Interfaces* **2020**, *12* (30), 33710−33718.
(27) Yao, Y. X.; Chen, X.; Yan, C.; Zhang, X. Q.; Cai, W. L.; Huang, J. Q.; Zhang, Q. Regulating Interfacial Chemistry in Lithium-Ion Batteries by a Weakly Solvating Electrolyte**. *Angew. Chem., Int. Ed.* **2021**, *60* (8), 4090−4097.
(28) Zhou, T.; Zhao, Y.; El Kazzi, M.; Choi, J. W.; Coskun, A. Integrated Ring-Chain Design of a New Fluorinated Ether Solvent for High-Voltage Lithium-Metal Batteries. *Angew. Chem., Int. Ed.* **2022**, *61* (19), No. e202115884.
(29) Ren, X.; Gao, P.; Zou, L.; Jiao, S.; Cao, X.; Zhang, X.; Jia, H.; Engelhard, M. H.; Matthews, B. E.; Wu, H.; et al. Role of inner solvation sheath within salt-solvent complexes in tailoring electrode/electrolyte interphases for lithium metal batteries. *Proc. Natl. Acad. Sci. U. S. A.* **2020**, *117* (46), 28603−28613.
(30) Cao, X.; Jia, H.; Xu, W.; Zhang, J. G. Review-Localized High-Concentration Electrolytes for Lithium Batteries. *J. Electrochem. Soc.* **2021**, *168* (1), No. 010522.
(31) Cao, X.; Ren, X. D.; Zou, L. F.; Engelhard, M. H.; Huang, W.; Wang, H. S.; Matthews, B. E.; Lee, H.; Niu, C. J.; Arey, B. W.; et al. Monolithic solid-electrolyte interphases formed in fluorinated orthoformate-based electrolytes minimize Li depletion and pulverization. *Nat. Energy* **2019**, *4* (9), 796−805.
(32) Wang, Y.; Li, Z.; Hou, Y.; Hao, Z.; Zhang, Q.; Ni, Y.; Lu, Y.; Yan, Z.; Zhang, K.; Zhao, Q.; et al. Emerging electrolytes with fluorinated solvents for rechargeable lithium-based batteries. *Chem. Soc. Rev.* **2023**, *52* (8), 2713−2763.
(33) Cao, X.; Gao, P.; Ren, X.; Zou, L.; Engelhard, M. H.; Matthews, B. E.; Hu, J.; Niu, C.; Liu, D.; Arey, B. W.; et al. Effects of fluorinated solvents on electrolyte solvation structures and electrode/electrolyte interphases for lithium metal batteries. *Proc. Natl. Acad. Sci. U. S. A.* **2021**, *118* (9), No. e2020357118.
(34) Schelhaas, M.; Waldmann, H. Protecting group strategies in organic synthesis. *Angew. Chem., Int. Ed.* **1996**, *35* (18), 2056−2083.
(35) Cheng, M.; Guo, C. Y.; Gross, M. L. The Application of Fluorine-Containing Reagents in Structural Proteomics. *Angew. Chem., Int. Ed.* **2020**, *59* (15), 5880−5889.
(36) Yoo, D. J.; Yang, S.; Kim, K. J.; Choi, J. W. Fluorinated Aromatic Diluent for High-Performance Lithium Metal Batteries. *Angew. Chem., Int. Ed.* **2020**, *59* (35), 14869−14876.
(37) Zhao, Y.; Zhou, T.; Mensi, M.; Choi, J. W.; Coskun, A. Electrolyte engineering via ether solvent fluorination for developing stable non-aqueous lithium metal batteries. *Nat. Commun.* **2023**, *14* (1), 299.
(38) Yu, Z.; Rudnicki, P. E.; Zhang, Z. W.; Huang, Z. J.; Celik, H.; Oyakhire, S. T.; Chen, Y. L.; Kong, X.; Kim, S. C.; Xiao, X.; et al. Rational solvent molecule tuning for high-performance lithium metal battery electrolytes. *Nat. Energy* **2022**, *7* (1), 94−106.
(39) Zhao, Y.; Zhou, T. H.; Jeurgens, L. P. H.; Kong, X.; Choi, J. W.; Coskun, A. Electrolyte engineering for highly inorganic solid electrolyte interphase in high-performance lithium metal batteries. *Chem.* **2023**, *9* (3), 682−697.
(40) Chen, S.; Yu, Z.; Gordin, M. L.; Yi, R.; Song, J.; Wang, D. A Fluorinated Ether Electrolyte Enabled High Performance Prelithiated Graphite/Sulfur Batteries. *ACS Appl. Mater. Interfaces* **2017**, *9* (8), 6959−6966.
(41) Ren, X. D.; Zou, L. F.; Cao, X.; Engelhard, M. H.; Liu, W.; Burton, S. D.; Lee, H.; Niu, C. J.; Matthews, B. E.; Zhu, Z. H.; et al. Enabling High-Voltage Lithium-Metal Batteries under Practical Conditions. *Joule* **2019**, *3* (7), 1662−1676.
(42) Park, E.; Park, J.; Lee, K.; Zhao, Y.; Zhou, T.; Park, G.; Jeong, M.-G.; Choi, M.; Yoo, D.-J.; Jung, H.-G.; et al. Exploiting the Steric Effect and Low Dielectric Constant of 1,2-Dimethoxypropane for 4.3 V Lithium Metal Batteries. *ACS Energy Lett.* **2023**, *8* (1), 179−188.
(43) Fawdon, J.; Ihli, J.; Mantia, F.; Pasta, M. Characterising lithium-ion electrolytes via operando Raman microspectroscopy. *Nat. Commun.* **2021**, *12* (1), 4053.
(44) Wang, J.; Yamada, Y.; Sodeyama, K.; Chiang, C. H.; Tateyama, Y.; Yamada, A. Superconcentrated electrolytes for a high-voltage lithium-ion battery. *Nat. Commun.* **2016**, *7*, 12032.
(45) Li, T.; Zhang, X. Q.; Yao, N.; Yao, Y. X.; Hou, L. P.; Chen, X.; Zhou, M. Y.; Huang, J. Q.; Zhang, Q. Stable Anion-Derived Solid Electrolyte Interphase in Lithium Metal Batteries. *Angew. Chem., Int. Ed.* **2021**, *60* (42), 22683−22687.
(46) Jiang, L. L.; Yan, C.; Yao, Y. X.; Cai, W.; Huang, J. Q.; Zhang, Q. Inhibiting Solvent Co-Intercalation in a Graphite Anode by a Localized High-Concentration Electrolyte in Fast-Charging Batteries. *Angew. Chem., Int. Ed.* **2021**, *60* (7), 3402−3406.
(47) Shi, J.; Xu, C.; Lai, J.; Li, Z.; Zhang, Y.; Liu, Y.; Ding, K.; Cai, Y. P.; Shang, R.; Zheng, Q. An Amphiphilic Molecule-Regulated Core-Shell-Solvation Electrolyte for Li-Metal Batteries at Ultra-Low Temperature. *Angew. Chem., Int. Ed.* **2023**, *62* (13), No. e202218151.
(48) He, J.; Bhargav, A.; Shin, W.; Manthiram, A. Stable Dendrite-Free Sodium-Sulfur Batteries Enabled by a Localized High-Concentration Electrolyte. *J. Am. Chem. Soc.* **2021**, *143* (48), 20241−20248.

(49) Wang, Y. Separator Wettability Enhanced by Electrolyte Additive to Boost the Electrochemical Performance of Lithium Metal Batteries. *Nano-Micro Lett.* **2021**, *13* (1), 210.
(50) Shin, W.; Manthiram, A. A Facile Potential Hold Method for Fostering an Inorganic Solid-Electrolyte Interphase for Anode-Free Lithium-Metal Batteries. *Angew. Chem., Int. Ed.* **2022**, *61* (13), No. e202115909.
(51) Adams, B. D.; Zheng, J.; Ren, X.; Xu, W.; Zhang, J. G. Accurate Determination of Coulombic Efficiency for Lithium Metal Anodes and Lithium Metal Batteries. *Adv. Energy Mater.* **2018**, *8* (7), No. 1702097.
(52) Zheng, Q. F.; Yamada, Y.; Shang, R.; Ko, S.; Lee, Y. Y.; Kim, K.; Nakamura, E.; Yamada, A. A cyclic phosphate-based battery electrolyte for high voltage and safe operation. *Nat. Energy* **2020**, *5* (4), 291−298.
(53) Yamada, Y.; Chiang, C. H.; Sodeyama, K.; Wang, J. H.; Tateyama, Y.; Yamada, A. Corrosion Prevention Mechanism of Aluminum Metal in Superconcentrated Electrolytes. *ChemElectroChem.* **2015**, *2* (11), 1687−1694.
(54) Guo, R.; Gallant, B. M. Li_2O Solid Electrolyte Interphase: Probing Transport Properties at the Chemical Potential of Lithium. *Chem. Mater.* **2020**, *32* (13), 5525−5533.
(55) Orlova, E. D.; Savina, A. A.; Abakumov, S. A.; Morozov, A. V.; Abakumov, A. M. Comprehensive Study of Li^+/Ni^{2+} Disorder in Ni-Rich NMCs Cathodes for Li-Ion Batteries. *Symmetry* **2021**, *13* (9), 1628.
(56) Li, T. Y.; Yuan, X. Z.; Zhang, L.; Song, D. T.; Shi, K. Y.; Bock, C. Degradation Mechanisms and Mitigation Strategies of Nickel-Rich NMC-Based Lithium-Ion Batteries. *Electrochem. Energy Rev.* **2020**, *3* (1), 43−80.
(57) Nam, G. W.; Park, N. Y.; Park, K. J.; Yang, J.; Liu, J.; Yoon, C. S.; Sun, Y. K. Capacity Fading of Ni-Rich NCA Cathodes: Effect of Microcracking Extent. *ACS Energy Lett.* **2019**, *4* (12), 2995−3001.
(58) Ryu, H. H.; Park, K. J.; Yoon, C. S.; Sun, Y. K. Capacity Fading of Ni-Rich $Li[Ni_xCo_yMn_{1-x-y}]O_2 (0.6 \leq x \leq 0.95)$ Cathodes for High-Energy-Density Lithium-Ion Batteries: Bulk or Surface Degradation? *Chem. Mater.* **2018**, *30* (3), 1155−1163.
(59) Wu, F.; Liu, N.; Chen, L.; Su, Y. F.; Tan, G. Q.; Bao, L. Y.; Zhang, Q. Y.; Lu, Y.; Wang, J.; Chen, S.; et al. Improving the reversibility of the H2-H3 phase transitions for layered Ni-rich oxide cathode towards retarded structural transition and enhanced cycle stability. *Nano Energy* **2019**, *59*, 50−57.